



Cell Motility and the Cytoskeleton Video Supplement 5

Explorations in Cell Motility

Video Tape Contents

	Time Start
1. Titles	0:00
2. Prologue	0:19
3. Occurrence of Fibers and Their Association With Talin in the Cleavage Furrow of PtK2 Cells Jean M. Sanger, Jeffery S. Dome, Rick S. Hock, Balraj Mittal, and Joseph W. Sanger	1:04
4. Interactions of <i>Listeria Monocytogenes</i> With Infected Host Cells Jean M. Sanger, Frederick G. Dold, Dipali Nanavati, and Joseph W. Sanger	7:54
5. Fertilization and Pronuclear Migration in the Ctenophore, <i>Beroe ovata</i> Christian Sardet, Christian Rouvière, Danielle Carré, Patrick Chang, and Evelyn Houliston	17:49
6. Measurement of Traction Forces in Cells Locomoting Along a Substratum Tim Oliver, Micah Dembo, and Ken Jacobson	25:49
7. Computer Modeling of the Ciliary Axoneme Michael Holwill, Guy Foster, Ernestina Guevara, Toshikazu Hamasaki, and Peter Satir	35:36
8. Actin-based Vesicle Dynamics and Exocytosis During Wound Wall Formation in Characean Internodal Cells Ilse Foissner, Irene K. Lichtscheidl, and Geoffrey O. Wasteneys	48:35
9. Three Flagellar Motilities in <i>Chlamydomonas</i> Unrelated to Flagellar Beating Keith G. Kozminski, Paul Forscher, and Joel L. Rosenbaum	54:53
10. Acknowledgments	59:18

1. TITLES

Video Supplement Number 5

Video Editors

Jean M. Sanger
Joseph W. Sanger

Consultant
Shinya Inoué

2. PROLOGUE

Motility is an essential and varied aspect of life. From the locomotion of whole organisms to intracellular movements, the complexity as well as the beauty of the motility can be observed in moving images. Observation of the motility is the first step in understanding the bases for the diverse methods that cells use to generate these movements. The properties of these movements can be analyzed by a variety of techniques. This video supplement for *Cell Motility and the Cytoskeleton* presents dynamic sequences that the printed page cannot convey. The details of the experiments shown here are in the references cited in each chapter on this video supplement.

3. OCCURRENCE OF FIBERS AND THEIR ASSOCIATION WITH TALIN IN THE CLEAVAGE FURROW OF PtK2 CELLS

Jean M. Sanger, Jeffery S. Dome, Rick S. Hock, Balraj Mittal, and Joseph W. Sanger

Cell Motility and the Cytoskeleton 27:26–40, 1994

Phalloidin Injections

Interphase cell. When interphase cells are microinjected with trace amounts of fluorescently labeled phalloidin, the probe binds to the actin filaments of the stress fibers in a periodic pattern.

Bipolar mitotic cell. When an injected interphase cell enters prophase, the stress fibers disassemble, leaving a uniform distribution of fluorescence throughout the cell. During anaphase, actin filaments concentrate in the cleavage furrow. The concentration of actin decreases during cytokinesis. The two new daughter cells spread and stress fibers reform during interphase. This cytokinesis sequence is reversed and repeated to demonstrate the dynamic changes in the actin filaments.

In this flat mitotic cell, the diffuse distribution of the fluorescent probe, phalloidin, rearranges into a cleavage furrow that is composed of distinct actin fibers (Fig. 1). As the cleavage furrow contracts, the actin bundles become thicker and brighter. When the two daughter cells enter interphase, the array of stress fibers starts to reform.

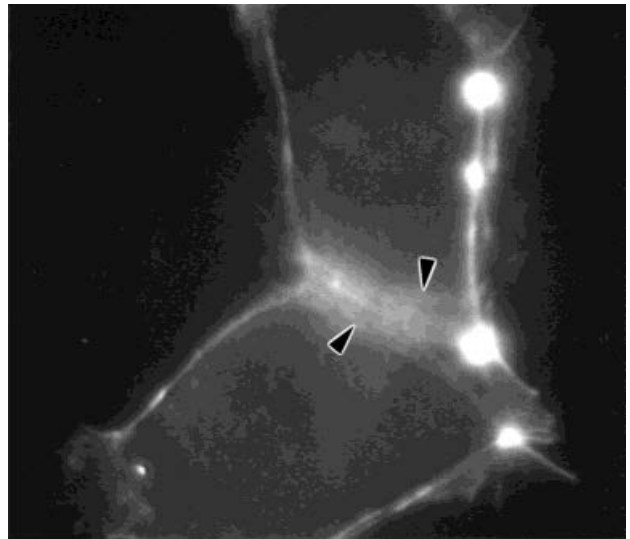


Fig. 1. A single time point from the video of a PtK2 previously injected during interphase with rhodamine-labeled phalloidin. The interphase stress fibers have disassembled. Distinct actin fibers (*arrowheads*) have assembled in the cleavage furrow of this bipolar cell.

This sequence is reversed and repeated to demonstrate the formation of the actin fibers in the furrow region and their participation in the contraction process.

Tripolar mitotic cell. The most complex patterns of actin fibers in cleavage furrows are observed in cells with multiple mitotic poles. In the three cleavage furrows that form among the three sets of separating chromosomes in this cell, actin fibers become aligned in the multiple furrows to form an interconnected contractile network. The sequence of cytokinesis is reversed and repeated in this cell to illustrate the complex interactions of the contracting fibers.

Tetrapolar mitotic cell. The fluorescent and phase-contrast images of this tetrapolar cell are paired to illustrate the position of the chromosomes and the actin fibers forming between the four sets of separating chromosomes. The process of cytokinesis is repeated.

Myosin Light Chains

Interphase cell. When microinjected into cells, fluorescently labeled myosin light chains are incorporated into the native myosin molecules and distributed in a periodic or sarcomeric array along the stress fibers, as in this interphase cell.

Tripolar mitotic cell. The fibers that assemble in the areas among the three sets of separating chromosomes in this cell contain fluorescent myosin light chains. Sometimes periodic distributions of myosin can be detected in the contracting fibers of the furrows.

Talin

Interphase cell. Stress fibers are attached to the cell surfaces by attachment plaques. Talin is an important

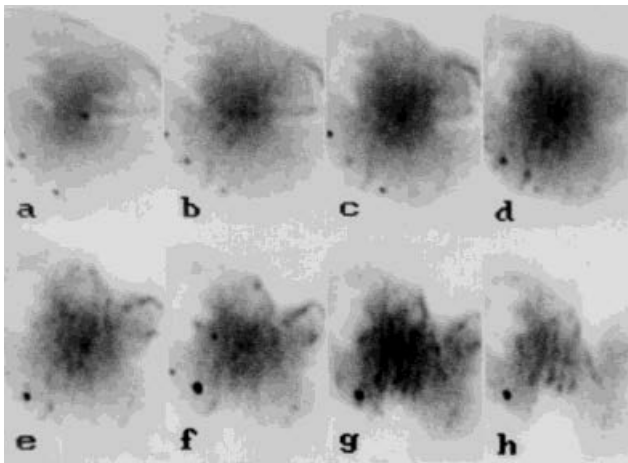


Fig. 2. A montage of time points from the video of a bipolar PtK2 cell previously injected with rhodamine labeled talin. The contrast has been inverted to emphasize the visibility of the attachment plaques forming in the cleavage furrow.

component of the attachment plaques. In interphase cells injected with fluorescently labeled talin, the probe is concentrated in the attachment plaques.

Bipolar mitotic cell. When the injected interphase cells enter mitosis, the stress fibers and their attachment plaques disassemble. During anaphase, the attachment plaques are assembled in the forming furrow region. The actin and myosin fibers are attached to the furrow membrane by these attachment plaques. The sequence is repeated with the contrast inverted (Fig. 2). These montages illustrate the formation of talin-containing attachment plaques in the furrow region.

Summary. This diagram summarizes images presented in this chapter and in the published work. Sarcomeric stress fibers in interphase cells disassemble as the cell enters mitosis. The fibers that assemble between the separating chromosomes during anaphase are banded in substructure. These fibers contract and disassemble during cytokinesis. The disassembled proteins are then recycled to form stress fibers in the two daughter cells. This work was supported by the National Science Foundation.

4. INTERACTIONS OF *LISTERIA MONOCYTOGENES* WITH INFECTED HOST CELLS

Jean M. Sanger, Frederick G. Dold, Dipali Nanavati, and Joseph W. Sanger

Cell Motility and the Cytoskeleton 28:97–107; 28, 346–358, 1994

Listeriosis. Listeriosis, or circling disease, in farm animals is due to infection by *Listeria monocytogenes*.

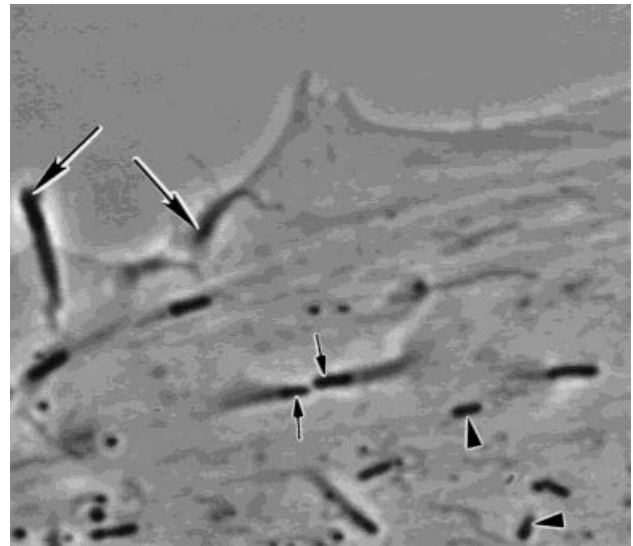


Fig. 3. A single time point from the video illustrating moving and nonmoving *Listeria monocytogenes* in an infected PtK2 cell. Note the two moving *Listeria* (small arrows) in the middle of the cell with phase dense tails passing by one another. The nonmoving bacteria (arrowheads) do not have tails of actin. Note the filopodia (large arrows) containing *Listeria* at their tips.

Listeria infect intestinal cells, macrophages and parts of the brain. This latter site of infection causes infected animals to walk in circles. This segment was taken by the late Dr. W.D. Boucher, University of Pennsylvania School of Veterinary Medicine.

Phase Contrast Sequences

Real-time movement. This infection process can be studied at the cell level in tissue culture. The *Listeria* are moving in this infected PtK2 cell at an average rate of 0.1 μm per second. A phase dense tail of actin and α -actinin is associated with the moving bacteria. The two moving *Listeria* in the middle of the cell can be observed to gracefully pass by one another (Fig. 3). The nonmoving bacteria do not have tails of actin. We know that new actin monomers are polymerized near the surfaces of the bacteria and that the newly formed filaments remain in place as the bacteria move forward. The actin filaments in the tail disassemble to supply subunits to be recycled back to the cytoplasmic pool. Bacteria near the surfaces have pushed out pieces of the cell to form filopodia. These filopodia undulate above the surface of the cell. The membrane encases the bacteria at the tips of the filopodia and the actin filaments projecting behind them.

Time-lapse movement. The following two sequences are played at about 100 times the real speed. Note the phase-dense tails of the moving *Listeria*, the formation of the filopodia, and the fusion of the filopodia with the cell surface, which allows the *Listeria* to reenter the main part of the same cell. These events are now shown in a different example.

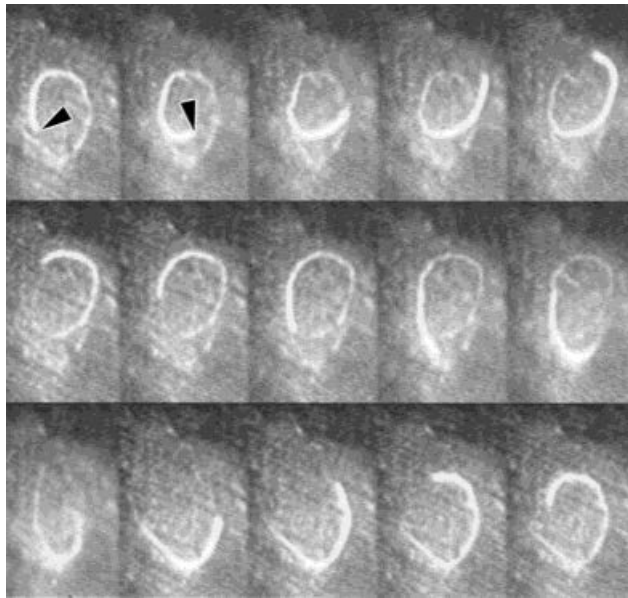


Fig. 4. Segmented images, shown sequentially, of an infected PtK2 cell previously microinjected with rhodamine-labeled alpha-actinin. Note that the oldest part of the tail appears as a fluorescent arc that remains stationary as the bacterium (arrowheads) moves forward and initiates the formation of new actin filaments cross-linked by alpha-actinin molecules. The newest segment of the tail is adjacent to the bacterium and is the brightest. The older parts of the tails disassemble their components back to the cytoplasmic pool. The bacterium is circling in a cloud of fluorescent alpha-actinin molecules released from the disassembly of the tails.

Injection of fluorescently labeled alpha-actinin.

Fluorescently labeled actin binding proteins such as alpha-actinin can be injected into host cells to allow the process of assembly and disassembly of the actin tails to be analyzed. The labeled probe is present in the normal stress fibers of this PtK2 cell as well as in the tails of the *Listeria*. Alpha-actinin cross-links the actin filaments on the surface of the bacterium as well as the tail. Contrary to first impressions, the actin filaments do not move with the bacterium but are left behind as the bacterium couples the polymerization of new actin polymers to its forward movements. In these segmented images, shown sequentially, the oldest part of the tail appears as a fluorescent arc that remains stationary as the bacterium moves forward and initiates the formation of new actin filaments. The newest segment of the tail is adjacent to the bacterium and is the brightest. The older parts of the tails disassemble their components back to the cytoplasmic pool. The bacterium is circling in a cloud of α -actinin released from the disassembly of the tails.

Fluctuations in speed during *Listeria* motility in host cell cytoplasm. As this graph of speed versus time shows, the speed of a single bacterium is not constant.

Long tails, short tails. Within the same infected cell here, injected with fluorescently labeled α -actinin,

some *Listeria* are stationary, the others move at different rates of speed. The faster moving bacteria initiate the polymerization of actin tails at a faster rate than those *Listeria* moving at a slower rate. Thus the faster moving bacteria have longer tails of actin and alpha-actinin than slower moving *Listeria*.

Bacterial Cell Division

Phase-contrast images. Moving bacteria are always associated with actin tails in the infected cell. The bacteria lose their tails when they divide. Tails will reform at the distal ends of their daughter bacteria. Note the dividing bacteria in the bottom center of the cell. As soon as the two daughters form tails, they move. The latter part of this sequence is played several times, to highlight the coupling of new actin tails to movement.

Fluorescent alpha-actinin injection cell. In this α -actinin injected cell, a stationary dividing cell is circled. The two daughter cells shortly couple the formation of new tails and movement away from one another. These two *Listeria* soon move away among the other *Listeria*. The same two daughters are shown at a higher magnification in reverse contrast. The individual images are played at a slower rate and are sometimes played backward to emphasize the coupling of new actin tails and the movement of the two daughter cells.

Microinjecting fragments of α -actinin. Injection of part of the α -actinin molecule leads to the inhibition of the movement of the intracellular *Listeria*. A few frames of normal movement before injection. Slight movement of 6 min after injection. No movements at 45 min postinjection. If the cell is stained with phalloidin and an α -actinin antibody, no tails are detected. The conclusion is that intact α -actinin molecules are needed for the normal movement of *Listeria* inside infected cells.

Summary. This model indicates that the forward movement of *Listeria* inside infected cells is coupled to the polymerization of actin monomers induced by actin nucleating proteins at the surface of the bacteria. The actin filaments are cross-linked and capped by other proteins to form the stationary tails. (This work was supported by the U.S. Department of Agriculture.)

5. FERTILIZATION AND PRONUCLEAR MIGRATION IN THE CTENOPHORE, *BEROE OVATA*

Christian Rouvière, Evelyn Houliston,
Danielle Carré, Patrick Chang,
and Christian Sardet

Cell Motility and the Cytoskeleton 29: 301–311, 1994

Beroe ovata are ctenophores (also called comb jellies) 5–20 cm in length. They can be collected from

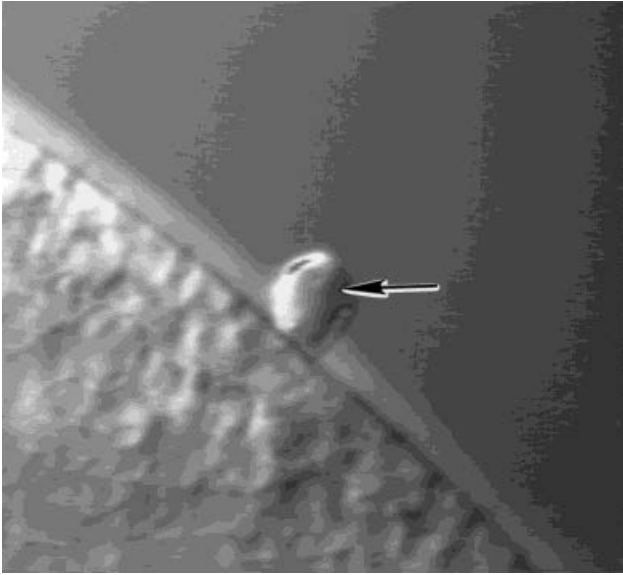


Fig. 5. A *Beroe* sperm (arrow) with its ovoid-shape nucleus is fusing with the surface of an egg.

February through May in the bay of Villefranche. Larvae and adults have eight rows of beating “comb plates of cilia” that develop within 2 days of fertilization. Ctenophores have only one axis of symmetry, the oral–aboral axis here running from right to left.

Beroe ovata eggs are ~1 mm in diameter and are characterized by a thin peripheral layer of fluorescent cytoplasm in which all cellular events occur. The egg is transparent, allowing fertilization to be observed with exceptional clarity. Here, we see a profile view of a sperm nucleus entering the egg after fusion (Fig. 5). The sequence is accelerated 100 times.

Now, we see the sperm as it fuses with the egg, provoking a localized contraction of the egg surface. This contraction normally lasts 2–3 min. One or several spermatozooids can penetrate the egg.

In this low-light-level, time-lapse sequence, the migrating female pronucleus, labeled with the DNA dye Hoechst 33342, leaves the site of meiosis to move toward one sperm-derived male pronucleus seen as a small white dot. The female nucleus sometimes changes direction and migrates to a neighboring male pronucleus.

After migrating toward the second male pronucleus, the female pronucleus enters the zone of accumulated organelles that surrounds the male pronucleus and pronuclear fusion occurs. At ~70 min after fusion, mitosis takes place. A unipolar cleavage furrow starts to bisect the egg ~2 hr after the onset of female pronuclear migration.

In this differential interference contrast sequence, accelerated 100 times, the female pronucleus migrates beneath the egg surface toward a stationary male pronucleus surrounded by a zone of accumulated organelles.

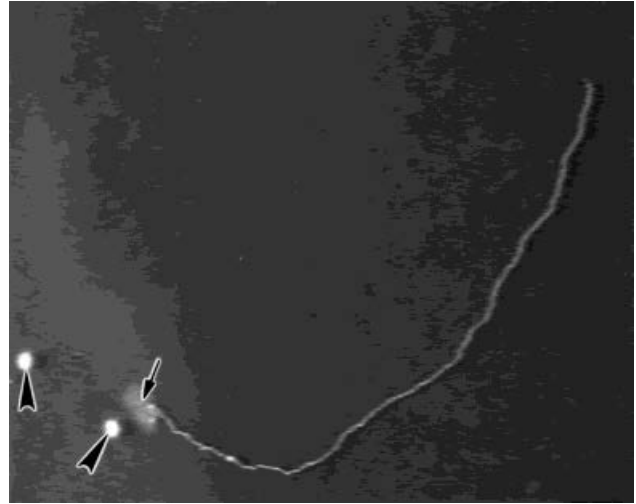


Fig. 6. Hoechst dye has been used to label the single egg pronucleus (arrow) and the two sperm pronuclei (arrowheads) in this part of the large *Beroe* egg. The trajectory of the migrating egg pronucleus is traced by following the labeled egg pronucleus using low light level recording. The egg pronucleus migrates toward a sperm pronucleus at a speed of ~0.2 $\mu\text{m}/\text{sec}$.

Mitosis occurs after the male and female pronuclei have fused. The mitotic spindle often forms with its long axis perpendicular to the direction of approach of the female pronucleus.

The female pronucleus causes the egg surface to bulge as it glides beneath it. The nuclear contents occasionally rotate but mostly translates while it moves. It usually slows down as it comes closer to the male pronucleus.

The trajectories of migrating nuclei can be examined using low light level recording of eggs incubated in Hoechst (Fig. 6). Here, the pronucleus migrates toward a sperm pronucleus at a speed of ~0.2 $\mu\text{m}/\text{sec}$.

If no sperm enter the egg, the female pronucleus migrates at random under the egg surface for several hours.

When several sperm pronuclei share a zone of accumulated organelles, the female pronucleus may approach the male pronuclei successively before fusing with one.

We have developed automated methods to analyze the trajectory and behavior of migrating nuclei.

This is another example of a female pronucleus hesitating before it fuses with one pronucleus.

In these differential interference contrast images, details of the fusion of the male and female pronuclei and the decondensation of the paternal chromatin after fusion can be observed.

Mitosis occurring just beneath the surface also can be visualized and analyzed. Note the oscillating spindle. This sequence is accelerated 150 times.

We have microinjected eggs with rhodamine-tubulin and observed the migration of the female pronucleus in dense sperm aster microtubules. These are consecutive images of a migrating nucleus in descending confocal sections.

The microtubules originate from each sperm centrosome forming very large flat asters beneath the egg surface. Egg and sperm pronuclei meet in the center of the aster and are seen here in successive confocal sections of a rhodamine-tubulin injected egg.

Starting at around the time of pronuclear fusion, a wave of cytoplasmic reorganization traverses the egg in ~ 30 min. Here the wave starts on the left of the egg where the pronuclei fuse. Following this wave, cytokinesis starts at the site of mitosis. A unipolar cleavage furrow bisects the egg in ~ 10 min. Three hours later, the eight blastomeres divide unequally. These cells have distinct compositions containing different proportion of internal and fluorescent peripheral cytoplasm. They have also distinct fates. For example, the smaller outer blastomeres are destined to form comb plates and the larger outer cells will differentiate into muscles.

REFERENCES IN THE VIDEO

Development 117:75–87.

Dev. Biol. 147:381–391.

Cell Motil. Cytoskeleton 29:301–311.

6. MEASUREMENT OF TRACTION FORCES IN CELLS LOCOMOTING ALONG A SUBSTRATUM

Tim Oliver, Micah Dembo, and Ken Jacobson

Cell Motility and the Cytoskeleton 31:225–240, 1995

Fish epidermal keratocytes demonstrate rapid, gliding locomotion, phase contrast, $36 \times$ real time (bar = $10 \mu\text{m}$). In this time lapse sequence, a typical fish epidermal keratocyte is seen locomoting. In contrast to fibroblasts, keratocytes exhibit a smooth gliding locomotion in which lamellipodial extension at the front of the cell and retraction at the rear occur simultaneously. Keratocytes have several features that are advantageous for studies of cell locomotion. They locomote spontaneously and rapidly at about one-third μm per second. They can maintain a constant velocity and direction for many minutes of observation, and they have a typically conserved shape and area. We are interested in traction forces generated by these and other rapidly locomoting cells.

Epidermal sheet spontaneously explants from fish scale in culture, $300 \times$ real time, phase contrast (bar = $50 \mu\text{m}$). If we immobilize a goldfish scale in culture medium, it will spontaneously explant an epidermal sheet, composed mainly of keratocytes, in ~ 18 hr. In this 50-min sequence, activity within the explant as well

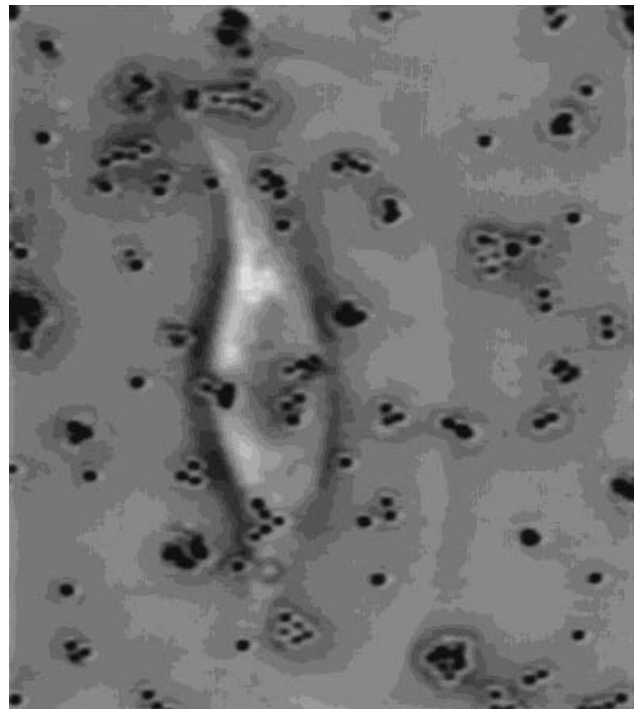


Fig. 7. A single keratocyte moving on a “hypercompliant” film. The cell is capable of moving beads substantial distances, in a pattern that is symmetric about the cell’s axis of locomotion.

as the migration of individual cells at its periphery can be seen.

Fish scale epidermis shows wound closure in 40 min, $150 \times$ real time, phase contrast (bar = $50 \mu\text{m}$). Such an epidermal explant demonstrates rapid wound healing in response to injury with a glass microneedle. The wound is almost completely healed over the course of this 40-min sequence.

Strong traction forces generated by epithelium, visualized on silicone rubber substratum, $150 \times$ real time, phase contrast (bar = $50 \mu\text{m}$). The cumulative traction forces generated by this epidermis can be visualized when the cell sheet is explanted onto a flexible substratum. Here ($300 \times$ real time), a highly crosslinked silicone rubber film is rearranged into the characteristic wrinkles first described by Harris.

Keratocyte locomoting on “hypercompliant” substratum, $30 \times$ real time, DIC imaging (bar = $20 \mu\text{m}$). In our modification of the traction force assay, we have designed a more weakly crosslinked film that stretches instead of wrinkling and incorporates latex beads as indicators of the film’s redistribution. In this particular film, which we describe as “hypercompliant,” a single keratocyte is capable of moving beads substantial distances, in a pattern that is symmetric about the cell’s axis of locomotion (Fig. 7).

Tracking bead centroids. A pair of beads approximately equidistant from the axis illustrates this symmetry and reports the strong traction forces generated by the cell's lateral lamellipodia, and directed towards the nucleus. Note also the whirlpools or vortices of beads created in the wake of the cell.

On-axis beads such as those illustrated here, follow a rearward path as they fall beneath the cell, with only minor deviations from the axis. Subsequent experiments suggested that this represents the film's reaction to a forward displacement by the cell, which occurred prior to the start of video-recording.

In this steady-state pattern of cell locomotion, we can see phase differences in the trajectories of beads along the cell's axis of locomotion. Beads on the left are in recovery phase; those on the right are beginning their motion. The incomplete return of beads to their starting positions is a consequence of both the recording time and area sampled, as well as a plastic element to the film's behavior.

Tracking beads "pushed" on another hypercompliant substratum, 30 × real time, DIC imaging (bar = 20 μm). If we start recording earlier, we can see beads displaced forward, several cell widths ahead of the kerocyte. The cell in this sequence is smaller, and beads make shorter paths but show a more complete return to their undisturbed positions. The movement of beads around triangular or circular paths shows a close correlation with the phases of cell locomotion. An initial push forward is followed by the arrival of the leading lamellipodium; then, a centripetal motion beneath the cell, followed by a recovery phase as the bead emerges from behind the cell.

Animation of bead trajectories, 100 × real time, (bar = 10 mm). Data from the previous sequence have been animated here to more clearly show the relationship between the moving beads and cell centroid. First the motion of the beads is represented as simple tracks or trajectories.

Dynamics of bead vectors. We can also represent a bead's motion at any time point as a line joining its current position with its undisturbed position. These bead vectors report the changing size and direction of traction forces exerted by the cell. Strong forces perpendicular to the cell's axis are apparent beneath both lateral lamellipodia. In a static display, we compile bead vectors into a map. Here, the cell's position is fixed and the progression of bead displacements is followed from right to left, over ~5 min of locomotion.

Mapping traction forces from locomotion on a more elastic substratum, 480 × real time, phase contrast (bar = 20 μm). If we cross-link the film even more, we create a more elastic substratum in which we can only just detect bead displacements reported by cell

traction forces. Locomotion is shown here in reverse loop time lapse. This elastic film behaves more closely in accordance with simple elasticity theory than our previous films, which makes the traction assay amenable to a quantitative analysis. From a pair of images representing the undisturbed and redistributed states of the film, we record bead locations and their subsequent displacements (Fig. 7).

Next, we can map these bead displacements at one time point. Input to the analysis is the bead displacements and a mesh of quadrilaterals, not shown here, superimposed on the cell. We compare this initial map to a second map of displacements predicted by the program. Finally, we minimize the difference between the two bead displacement maps to determine the traction density at each node of our cell mesh. The analysis shows traction beneath the entire cell, arranged as a symmetric pair of pincer-like gradients, along the cell's equator. Each gradient decreases in magnitude toward the cell center and is oriented perpendicular to the cell's axis.

Micromanipulation of beads in the elastic silicone rubber, 90 × real time, phase contrast (bar = 50 μm). To calibrate the traction assay, we deform the film at discrete loci with calibrated microneedles. Within the white rectangle, we see the trial of a single bead over a path of ~60 μm. The bead makes an almost complete recovery of its undisturbed position upon release. From a set of trials, we can show that the relationship between applied force and distance moved is highly linear for these elastic films. Our estimate for the maximum traction force applied by a keratocyte to flexible substrata is in the millidyne range.

Locomoting cell bending a needle, 60 × real time, phase contrast (bar = 20 μm). Another way to directly measure the resultant traction force exerted by a locomoting cell is shown here. The tip of a microneedle, suspended in the path of a cell is carried forward against the resistive force of its bending (Fig. 8). A very flexible needle, like this uncalibrated one, presents a seemingly negligible load to the cell, but demonstrates the principle of force measurement as it recoils to its starting position upon release.

The same needle (100 × real time) pressed against the substratum can be moved against its resistive force of friction by a locomoting cell. The thin lamellipodium slips beneath the obstacle until the cell nucleus is obstructed. At this time the needle is carried forward by first one cell, then conveniently a second. Loose bacteria on the substratum are also cleared from the path of the cell by its leading lamellipodium.

Measuring traction force from needle bending, 30 × real time, phase contrast (bar = 20 μm). The calibrated needle we have used to estimate traction forces in this "needle-drag" assay (Fig. 8) is stiffer than in the

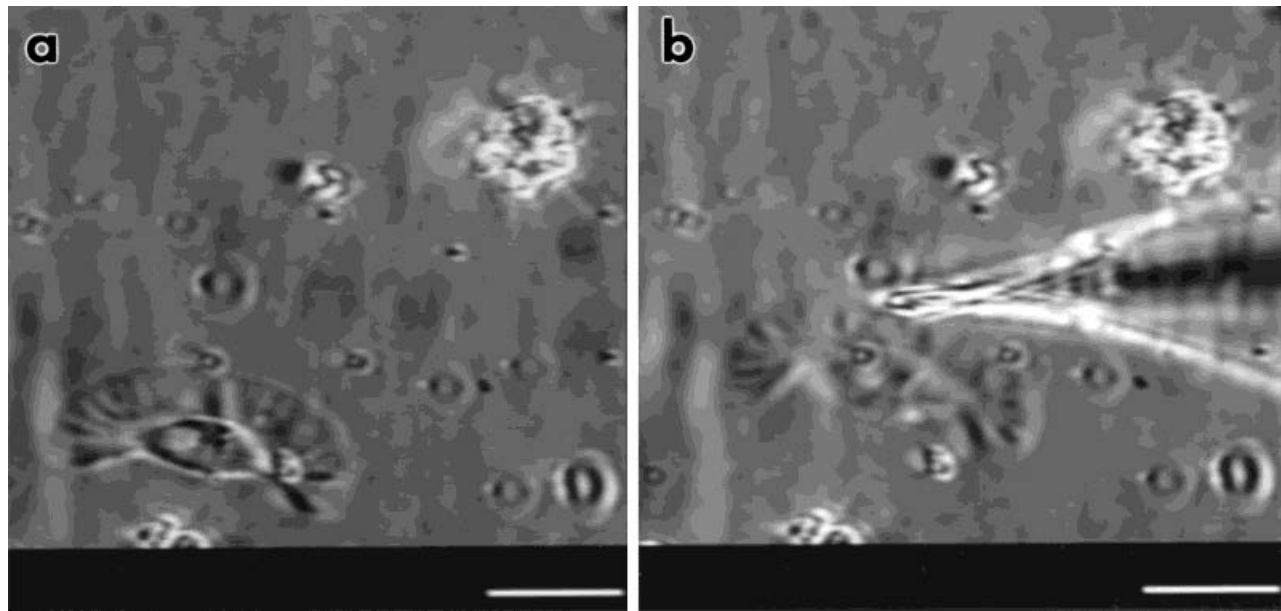


Fig. 8. (a) A fish keratocyte migrating on the substrate. (b) The tip of a microneedle is placed in the path of the same locomoting cell. The tip is carried forward by the keratocyte against the resistive force of the bending needle. A very flexible needle, like this uncalibrated one, presents a seemingly negligible load to the cell, but demonstrates the principle of force measurement as it recoils to its starting position upon release. Bar = 20 μm .

previous sequence. Such an obstacle presents a significant load to the cell, which it tries to avoid in a bifurcation of its lamellipodium. The cell is briefly stalled in its locomotion and carries the needle tip forward until it circumvents the obstacle. In a set of experiments like this, we measured resultant traction forces in the millidyne range. This is consistent with estimates of traction forces from our silicone rubber traction assay.

7. COMPUTER MODELLING OF THE CILIARY AXONEME

Michael Holwill, Guy Foster, Ernestina Guevara, Toshikazu Hamasaki, and Peter Satir

Cell Motility and the Cytoskeleton 32:114–120, 1995

This work, reported in volume 32 of *Cell Motility and the Cytoskeleton*, is an extension of the modeling of axonemes at macromolecular resolution presented by Sugrue et al. [1991].

The software package used to generate the model is called SURREAL—Surface Rendering Algorithms—and was written by Dr. A.N. Glazzard, now of 5D Ltd., specifically to model the axoneme. The package consists of a set of subroutines written in Fortran 77 and is capable of generating a scene from a range of primitive structures. To generate the axoneme, the main primitive structures used are the sphere and the polygon. SURREAL objects can be moved to any point in a scene by geometrical

transformations. A scene may be composed by bringing together smaller objects to construct a larger one.

To illustrate this, we show how a microtubule is built up from spheres with a diameter of 4 nanometres, appropriately scaled, each representing a tubulin subunit. The microtubule wall structure is built up by translating the spheres to generate a doublet structure consistent with that based on high resolution electron microscopy reported by Song and Mandelkow [1995], and others. The alpha and beta subunits are shown in blue and off-white. When placed vertically on the screen, as shown, the fast-growing, or plus-end, of the microtubule, which corresponds to the tip of the axoneme, is at the top of the screen. For the purposes of modeling, the dynamics of microtubule polymerization are not accurately reproduced in this construction, although the model is sufficiently versatile to allow this to be done. A doublet of any desired length—in this case $\sim 0.3 \mu\text{m}$ —can be generated.

The outer dynein arm is modeled after Barkalow et al. [1994a,b] and is appropriately positioned on the microtubule lattice. The inner arm structure shown, which is based on Sugrue et al. [1991], does not take into account its complexity as now understood. For convenience, the inner arm is represented as the mirror image of the outer arm.

Other structures, namely, the spoke groups, the interdoubtlet links, and the attachment sites of the microtubule–membrane links are added to complete the microtu-

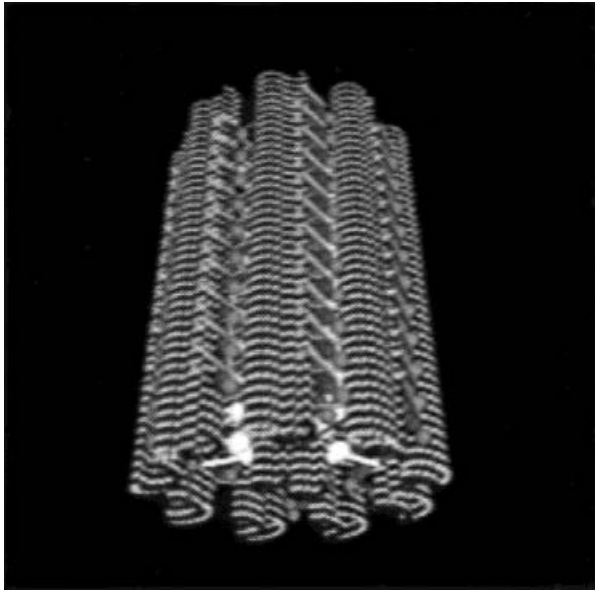


Fig. 9. A computer model of the longitudinal aspect of an axoneme. The original computer model is in color.

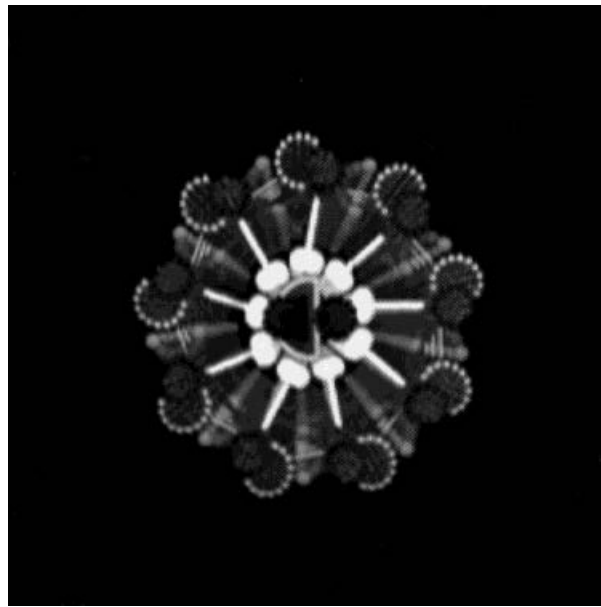


Fig. 10. A computer model of the cross-section of the axoneme. The original computer model is in color.

bule. Color is used to distinguish major components, with, e.g., the spokes in yellow and tubulin in blue.

By repeated appropriate translation and rotation of the microtubule, and the inclusion of the central complex, the model of the axoneme is generated.

The SURREAL reconstruction allows us to capture the axoneme in any desired position (Fig. 9). Rotations as seen in this sequence are programmed into the computer to produce a full 360° rotation about an axis perpendicular to the long axis of the axoneme (Fig. 10), together with a partial rotation about the long axis. The rotation gives the model a palpable sense of reality and can be used to represent the axoneme viewed from any direction for comparison with high-resolution electron micrographs as shown in Sugrue et al. [1991]. Selection of appropriate perspectives allows the model to be compared with thick sections of axoneme, such as those used for tomographic studies, with tomographic reconstructions themselves, with negative-stain images of axonemes and with some freeze-etch images.

Dynein arm cycle. The next objective is to add the dynamic properties of the axoneme to show how the various structures behave in detail during ciliary activity.

We began with the mechanochemical cycle of the outer dynein arm, which is important in the control of ciliary beat frequency and doublet microtubule sliding velocity. The structure of the outer dynein arm is essentially a compact form of the three-headed bouquet seen in protozoa. According to Barkalow et al. [1994a,b], the outer dynein arm is arranged transversely across the interdoubt gap, with a globular head (purple) projecting

outward, a body consisting of two additional head domains (red) and a cape (green) of intertwined stalks attached to the wall of the A-microtubule. The configuration of the arms may vary in electron micrographs to give five positions defined by Avolio et al. [1986]. As shown here, these positions can be arranged in a sequence corresponding to the mechanochemical cycle of the outer dynein arm that causes sliding between adjacent microtubules in the axoneme.

In this simulation, viewed from four different directions, the outer arm cycle contains five distinct phases, each linking successive positions in the sequence and each occupying the same amount of time. The force-producing step, or duty phase, occurs when the arm attaches strongly to the adjacent microtubule and moves vertically, in this simulation, to a rigor-like position that completes the cycle. To identify the duty phase in this and following simulations, we show the interacting head in yellow during the force producing step.

In this sequence showing the arm cycle, the timing of the duty phase has been altered to reflect the information presented by Hamasaki et al. [1995], which suggests that the duty phase occupies $\sim 1\%$ of the total cycle time.

Microtubule sliding. In the next sequences we consider how the activity of multiple dynein arms might generate microtubule sliding. It has previously been thought that the arm activity is coordinated in a sequential manner, but in vitro microtubule translocation experiments make an alternative model, where dynein arm activity is stochastic, more attractive. We have found it practical to use a doublet sliding simulation to model the

activity. The data obtained can, however, be compared directly to the results of Hamasaki et al. [1995].

The sliding model has the following assumptions: (1) dynein arm activity is stochastic, (2) the system behaves as if it were unloaded, (3) the step size for each dynein arm is the same—16 nanometers, (4) the arms act independently of each other, and (5) geometry of arm attachment is maintained in the translocating microtubule because dynein interacts weakly with the overlying microtubule when generating force. In the intact cilium, other structures, such as interdoubtlet links might also maintain the appropriate geometry.

In the simulation, the behaviour of the system is shown during a time equal to one arm cycle. The cycle time was divided into 100 equal segments. At the beginning of each time segment, the activity of each dynein arm was determined by a random number generator. In the sequences, the length of the active microtubule, N , is set at 15 dynein arm periods, and the driven microtubule, $N + 1$, has sufficient length that all the dynein arms can interact with it throughout the simulation. The displacement of microtubule $N + 1$ is indicated by the localized group of tubulin dimers coloured in yellow. The random nature of the arm activity is readily apparent and gives rise to the stepwise character of the microtubule displacement.

The sequence is repeated with a graph plotting the actual displacement against time to show the steps. We indicate the activity of a single arm in the side panel. This arm completes one cycle during the simulation. Because of the stochastic nature of the arm activity, each time the simulation is run the stepping pattern is different; three different simulations are presented to illustrate this.

The simulations allow us to plot microtubule displacement against time for microtubules of different lengths and hence to determine the microtubule velocities. When microtubule velocity is plotted against microtubule length, a curve similar in form to a hyperbola is generated.

This result is consistent with the experimental data of Hamasaki et al. [1995], which shows that a hyperbola fits the plot of microtubule translocation velocity against microtubule length in *in vitro* translocation experiments over 22S dynein substrata after varying treatments.

The results of the simulations presented here are consistent with the experimental data, and the underlying assumptions therefore deserve continued rigorous modeling. The objective is to make a quantitative comparison between the simulation and the experiments, with a view to obtaining information about the molecular mechanism involved in translocation and its relation to the dynein arm cycle in the intact axoneme. We plan to build on these simulations, using information derived from interactions between the predictions of modeling and the experimen-

tal results, with the goal of developing a fully functional model of the axoneme.

Articles Referenced in the Videotape

- Avolio, J., Glazzard, A.N., Holwill, M.E.J., and Satir, P. (1986): Structures attached to doublet microtubules of cilia: computer modelling of thin-section and negative-stain stereo images. *Proc. Natl. Acad. Sci. USA* 83:4808–4808.
- Barkalow, K., Hamasaki, T., and Satir, P. (1994a): Regulation of 22S dynein by a 29 kD light chain. *J. Cell Biol.* 126:727–735.
- Barkalow, K., Avolio, J., Holwill, M.E.J., Hamasaki, T., and Satir, P. (1994b): Structural and geometrical constraints on the outer dynein arm *in situ*. *Cell Motil. Cytoskeleton* 27:299–312.
- Hamasaki, T., Holwill, M.E.J., Barkalow, K., and Satir, P. (1995): Mechanochemical aspects of axonemal dynein activity studied by *in vitro* microtubule translocation. *Biophys. J.* 69:2569–2579.
- Song, Y.H., and Mandelkow, E. (1995): Recombinant kinesin motor domain binds to beta-tubulin and decorates microtubules with a B surface lattice. *Proc. Natl. Acad. Sci. USA* 90:1671–1675.
- Sugrue, P., Avolio, J., Satir, P. and Holwill, M.E.J. (1991): Computer modelling of Tetrahymena axonemes at macrotubular resolution: Interpretation of electron micrographs. *J. Cell Sci.* 59:5–16.

8. ACTIN-BASED VESICLE DYNAMICS AND EXOCYTOSIS DURING WOUND WALL FORMATION

Ilse Foissner, Irene K. Lichtscheidl, and Geoffrey O. Wasteneys

Cell Motility and the Cytoskeleton 35:35–48, 1996

Video-enhanced light microscopy of characean internodal cells. Vesicle dynamics in unwounded cells.

The rotational streaming of characean internodes involves interaction of myosin-coated organelles with actin filament bundles. The bundles are attached to the inner surface of stationary chloroplasts, which are up to 8 micrometers long (Fig. 11). Vesicles have a maximum diameter of 500 nanometers. They travel unidirectionally at velocities between 12 and 28 μm per second when in close contact with the bundles. In the endoplasm, vesicles and other organelles move in the same direction but at a higher velocity of $\sim 50 \mu\text{m}$ per second.

Vesicle dynamics in wounded cells. Injury by puncturing causes detachment of chloroplasts and local arrest of bulk streaming. Vesicles accumulate at the wound region and perform saltatory movements in all directions interspersed by oscillating movements and periods of complete immobility at the cell membrane.

Vesicle density and dynamics is highest near fast growing fibrillar wound walls (ww). At these sites, vesicle outlines overlap, which impedes detailed analysis.

The number of vesicles and their dynamics is lower at slowly or nongrowing wound walls (ww). Vesicles often adhere to the cell membrane for as long as 30 min before detaching.

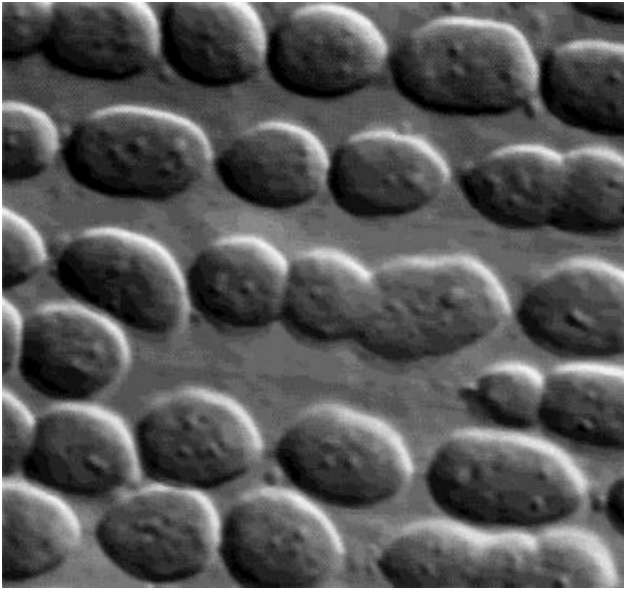


Fig. 11. These rows of chloroplasts are attached to one another by bundles of actin filaments. The original image is in color.

The best optical conditions for the study of vesicle behavior are found at the wound perimeter, where chloroplasts had detached slightly.

Occasionally, space is restricted to a single layer of vesicles that could then only move in one plane parallel to the cell membrane.

Wound Wall Secretion

Slowly merging vesicles, 9 min after imaging. Following wounding by UV light irradiation, vesicles start to move from the endoplasm toward the cell membrane, where they perform saltatory and oscillating movements.

20 min after injury. Most vesicles return into the endoplasm, but some of them become immobile at the cell membrane.

30 min after injury. The outlines of these vesicles merge gradually within several minutes, forming the clumps that comprise the amorphous wound wall.

Bursting vesicles in the wound wall. Some of the vesicle-like structures, probably vesicle contents, remain visible within the wound wall, far apart from the dynamic cytoplasm. They dissolve suddenly within 80 msec, equal to the duration of two video frames.

Bursting vesicles at the cell membrane. At the cell membrane, vesicles marked with a V disappear within 80 msec soon after transport from the endoplasm via saltatory movements. This disappearance can be ascribed either to dissolution or to movement into another optical plane. The latter can be excluded because the underlying chloroplast blocks journeys in the Z-axis.

Vesicles, therefore, disappear due to spreading of their content. Note that this vesicle dissolves without prior immobilization (v).

Recovery. During recovery, actin filament bundles become evident in the wound area. Vesicles occasionally change from saltatory movements along invisible tracks to continuous unidirectional movements along bundles and vice versa.

Addresses: Institutes of Plant Physiology, University of Salzburg and the University of Vienna, Austria; Research School of Biological Sciences, Australian National University, Canberra, Australia.

9. THREE FLAGELLAR MOTILITIES IN *CHLAMYDOMONAS* UNRELATED TO FLAGELLAR BEATING

Keith G. Kozminski, Paul Forscher, and Joel L. Rosenbaum

Cell Motility and the Cytoskeleton:
Video Supplement 5, Chapter 9

All images seen in this 4-min video were observed with video-enhanced differential-interference contrast microscopy. All segments are in real time.

Three flagellar motilities unrelated to flagellar beating have been observed in the biflagellate green alga *Chlamydomonas*: bead translocation (Fig. 12a) [reviewed by Bloodgood 1990, 1992], gliding (Fig. 12b) [reviewed by Bloodgood, 1990, 1992], and tipping [Goodenough and Jurvich, 1978; reviewed by Goodenough, 1991]. Recently, a fourth nonbeat flagellar motility, referred to as intraflagellar transport (Fig. 12c), also has been observed in the flagella of *Chlamydomonas* [Kozminski et al., 1993]. Of these, bead translocation, gliding, and intraflagellar transport are shown in this video.

Bead translocation. The first segment shows the bidirectional translocation of polystyrene beads that are 0.3 μm in diameter, along the length of the flagellum, on the surface of the flagellar membrane. On average, bead translocation occurs at 1.5–2 μm per second in both directions along the length of the flagellum, which is $\sim 10 \mu\text{m}$ long [Bloodgood, 1977; Kozminski et al., 1993]. The cell shown is the paralyzed-flagella mutant of pf 18 of *C. reinhardtii*, which lacks the central pair microtubules. The vertical field in this segment is $\sim 20 \mu\text{m}$.

Gliding. The second segment shows gliding of whole cells by means of their flagella, $\sim 15\text{--}20 \mu\text{m}$, across a glass coverslip. The region with high refractive index between the flagella is the cell body. For gliding to occur, at least one flagellum must be in contact with the substrate. Gliding occurs, on average, at 0.6–1 μm per second [Lewin, 1952; Bloodgood, 1981; Kozminski et

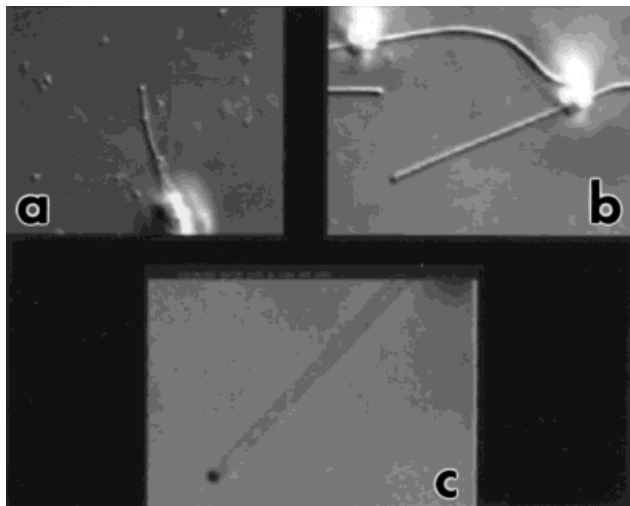


Fig. 12. Three different types of flagellar motilities are illustrated: (a) bead translocation, (b) gliding, (c) intraflagellar translocation.

al., 1993]. The cells shown are the paralyzed-flagella mutant M475 of *Chlamydomonas moewusii*. The vertical field in this segment is $\sim 20 \mu\text{m}$.

Intraflagellar transport. The third segment, which is repeated in the fourth segment, shows intraflagellar transport. Granule-like particles can be observed moving bidirectionally along the length of the flagellum. On average, movement to the flagellar tip occurs at $2.0 \mu\text{m}$ per second and to the flagellar base, at the highly birefringent cell body, at $3.5 \mu\text{m}$ per second in the M475 cells [Kozminski et al., 1993]. The vertical field is $\sim 20 \mu\text{m}$.

Intraflagellar transport. The fifth segment also shows intraflagellar transport in M475 cells, but the vertical field is $\sim 10 \mu\text{m}$.

All three motilities. The last segment shows all three motilities, bead translocation, gliding, and intraflagellar transport, occurring in the same M475 cell. The beads are $0.3 \mu\text{m}$ in diameter and the vertical field $\sim 30 \mu\text{m}$.

REFERENCES IN THE VIDEO

Bloodgood, R.A. (1977): Rapid motility occurring in association with the *Chlamydomonas* flagellar membrane. *J Cell Biol.* 75:983–989.

Bloodgood, R.A. (1981): Flagella-dependent gliding motility in *Chlamydomonas*. *Protoplasma* 106:183–192.

Bloodgood, R.A. (1990): Gliding motility and flagellar glycoprotein dynamics in *Chlamydomonas*. In Bloodgood, R.A. (ed.): “Ciliary and Flagellar Membranes.” New York: Plenum Press, pp. 91–128.

Bloodgood, R.A. (1992): Directed movements of ciliary and flagellar membrane components: A review. *Biol. Cell* 76:291–301.

Goodenough, U.W. (1991): *Chlamydomonas* mating interactions. In Dworkin, M. (ed.): Washington, DC: American Society for Microbiology, pp. 71–112.

Goodenough, U.W., and Jurivich, D. (1978): Tipping and mating-structure activation induced in *Chlamydomonas* gametes by flagellar membrane antiserum. *J Cell Biol.* 79:680–693.

Kozminski, K.G., Johnson, K.A., Forscher, P., and Rosenbaum, J.L. (1993): A motility in the eukaryotic flagellum unrelated to flagellar beating. *Proc. Natl. Acad. Sci. USA* 90:5519–5523.

Lewin, R.A. (1952): Studies in the flagella of algae. I. General observations of *Chlamydomonas moewusii* Gerloff. *Biol. Bull.* 103:74–79.

Address of authors: Department of Biology, Yale University, New Haven, CT 06520-8103.

10. ACKNOWLEDGMENTS.

Cell Motility and the Cytoskeleton

Producers

Jean M. Sanger
Joseph W. Sanger

Post Production

John M. Sanger

Special Thanks to:

The MARCOM Group Ltd.
Boothwyn, PA

The End